Identification of passive constitutive arterial tissue parameters from pressure myography based on inverse hyperelasticity

(original article)

Ali Fethi Okyar[a], Omer Faruk Buyukkaya[a], Cevat Volkan Karadag[a], Bilge Guvenc Tuna[b]

[a] *Faculty of Engineering, Yeditepe University, Atasehir, Istanbul, 34755, Turkiye*
[b] *Faculty of Medicine, Yeditepe University, Atasehir, Istanbul, 34755, Turkiye*

Abstract

Changes in the mechanical properties of arteries due to growth, remodeling, or aging are related with cardiovascular diseases. These changes can quantitatively be assessed if a suitable set of biomaterial constitutive parameters could be fitted onto the in vitro response from pressure myography. In Simon et al (1970), a pressure-diameter dataset reflecting the internal pressurization stage was provided. However, this data did not include the excised state. We developed an analytical continuum-based computational procedure to pull the current state back to the excised (reference) state. Using this procedure the data was fitted to a simple exponential model, and a 56% decrease in the shear modulus and a 19% decrease in the exponential constant were observed. Similar observations were made for the hyperelastic fibre-reinforced continuum model by Holzapfel et al (2000). In conclusion, the parameter identification process may be hindered as a result of an incomplete or partial dataset. Inverse deformation mapping may be used to produce the missing data.

Preprint submitted to Journal of the Mechanical Behavior of Biomedical Materials November 6, 2023

Keywords: soft-tissue biomechanics, parameter identification, inverse deformation, vasculatory system, hyperelasticity, finite element analysis
2000 MSC: 0000, 1111

1. Introduction

Cardiovascular diseases are directly related to changes in the mechanical properties of arteries due to growth, remodeling, or aging. (s. Roy, 1881; Heagerty et al., 1993; Hayashi, 1993; Sell and Monnier, 2012; Mitchell et al., 2007; Lakatta et al., 2009; Lee and Oh, 2010; Leblanc et al., 2018; Ungvari et al., 2018). These changes can quantitatively be assessed through the parameters of a suitable biomaterial constitutive model (see Mackerle (2005) and Wex et al. (2015) for comprehensive reviews on the subject) if they can be fitted onto in-vitro/in vivo response data. Among various experimental methods, pressure myography stands out as a practical and economical technique to measure the pressure-diameter response of arterial vessels subjected to internal pressure in ex vivo. Although there are many references that provide pressure-diameter data from pressure myography (s. Roy, 1881; Simon et al., 1971; Cheung and Hsiao, 1972; Vaishnav et al., 1973; Hayashi et al., 1974; Kas'yanov, 1974; Taira et al., 1974; Young et al., 1977; Fung et al., 1979; Vito and Hickey, 1980; Dobrin, 1984; Zulliger et al., 2004; Kang, 2008; Avril et al., 2010; Sleboda and Roberts, 2017; Ramachandra and Humphrey, 2019), it is not straightforward to compare their results due to difficulties arising from the differences in measurement units, test protocols, and even constitutive models.

We quote from Myneni and Rajagopal (2022) *"... we should look to de-*

veloping a sufficiently simple model that has some predictive capability, even if it is not faithful to the details of the tissue structure." In their two papers Simon et al. (1971, 1972) first presented the pressure-diameter response of a canine aortic artery, and then used this data to fit the parameters of a constitutive model that is sufficiently simple, as mentioned in Myneni and Rajagopal (2022).

Inverse elasticity provides a multi-faceted range of applications from estimating material parameters (Simon et al., 1971; Cheung and Hsiao, 1972; Demiray, 1972; Vaishnav et al., 1973; Mirsky, 1973; Hayashi et al., 1974; Kas'yanov, 1974; Young et al., 1977; Chuong and Fung, 1983; Wu et al., 1984; Chuong and Fung, 1986; Ogden et al., 2004; Holzapfel et al., 2004; Zulliger et al., 2004; Einstein et al., 2005; Wicker et al., 2008; Avril et al., 2010; Garcia-Gonzalez et al., 2018; Huh et al., 2019), to recovery of initial (residual) stress distribution and beyond. Inverse deformation analysis benefits from mathematical optimization tools to recover an unknown state of the body, based on a known configuration (Genovese, 2007, 2009; Avril et al., 2010; Morin and Avril, 2015; Mazier et al., 2022), while Avril et al. (2010) used full field optical measurements of human arteries in-vitro for parameter estimation.

Estimating biological constitutive parameters from experimental data may prove to be a rather challenging optimization problem due to the presence of material and configuration related non-linearities and unknowns. The most simplistic passive constitutive models have been proposed as a function of the first invariant of the right Cauchy deformation tensor, C_1 in their hyperelastic isotropic strain energy functionals, for example in Demiray (1972)

and Simon et al. (1972). On the other hand, more sophisticated constitutive models have recently appeared, such as the micro-mechanically based theory proposed in Holzapfel et al. (2000). However, the price of using such highly sophisticated constitutive models is increased complexity in the parameter estimation procedure, and a high likelihood of ending up with an overfitting problem.

We first derive in section 2.1, a continuum mechanics based pressure-diameter expression of an axisymmetrically extending inflating vessel geometry based on the micro-mechanically based constitutive model. Then, we describe in section 2.2, the procedure for estimating model parameters from experimental data by using an optimization function. The recovery of the excised (undeformed) configuration using the pull-back operation is explained in section 2.3. As a result, **we hypothesize that the potential difficulty posed by the variation in measurements or lack of data pertaining to the undeformed state which might lead to inaccurate parameter estimates can be averted by incorporating the pull-back operation a priori into the deformation cycle in the optimization routine.**

2. Theory and Methods

As put forth in the beginning of the prior section, there is a need for a good but sufficiently simple model description of the arterial constitutive making. The following relation was proposed by Simon et al. (1971) and Demiray (1972), independently but around the same time

$$\frac{\partial \mathscr{W}_s}{\partial I} = \mathscr{A}\, \mathrm{e}^{k(I-3)} \tag{1}$$

where $\partial \mathscr{W}_s/\partial I$ represents a mechanical property analogous to the shear modulus in the undeformed (natural) configuration. In case, the reference configuration is different from the undeformed configuration, the constant 3 in Eq. 1 may be replaced by I_0, the value taken by the invariant I in the new reference configuration. The rationale for modifying the SED function in such a way is due to the fact that the pressure-diameter data is recorded in the tethered configuration, which is obviously not the undeformed configuration. Indeed, in the tethered configuration, the vessel has been extended by an axial stretch of λ, and $I_0 = \lambda^2 + 2/\lambda$. We note here that, in Simon et al. (1972), such a modified SED function as described above has been utilized, and Eq.1 has been replaced by

$$\frac{\partial \mathscr{W}_{s'}}{\partial I} = \mathscr{A}\, \mathrm{e}^{k(I-I_0)} \tag{2}$$

This relation is directly utilized in the general form of the Cauchy stress components for an incompressible isotropic material for which the SED is only a function of the first invariant I of $\boldsymbol{C}$, which reads

$$\sigma_{rr} = -p + 2\frac{\partial \mathscr{W}_s}{\partial I}\lambda_r^2, \quad \sigma_{\theta\theta} = -p + 2\frac{\partial \mathscr{W}_s}{\partial I}\lambda_\theta^2 \tag{3}$$

where λ_r and λ_θ correspond to the principal stretches in the radial and circumferential directions, respectively (Holzapfel, 2000; Nair, 2009).

2.1. Continuum-based axisymmetric stress-stretch relations

Let $\mathscr{B}^0$ denote the excised (E) configuration of the vessel body in which a stress-free condition is assumed to prevail. Although the vessel axis may have

a slight curvature, we assume that it can be straightened with a negligible tethering load applied from its two ends. Thus, it becomes convenient to introduce a cylindrical coordinate system and mark the coordinates of a material point X as $\boldsymbol{X} = R\boldsymbol{e}_R + Z\boldsymbol{e}_Z$, where $\boldsymbol{e}_r$ and $\boldsymbol{e}_z$ denote the unit vectors in the radial and axial directions Irgens (2008). The inner and outer radii in this configuration are labeled as A and B, respectively.

In pressure-myography experiments the excised vessel is positioned between pressurization canulae and tethered by a certain amount of axial stretch, λ_z. In this intermediate configuration, $\mathscr{B}^T$, let the gauge section be defined as the portion of the vessel far enough from the canulae ends such that the strain distribution along the vessel axis is uniform. The material point X is now at $\bar{\boldsymbol{x}}$, and the inner and outer radii are, $\bar{a}$, and $\bar{b}$, respectively. In this and other configurations all relevant elastic fields in the gauge section will be taken as independent of the axial (Z) coordinate.

The final (inflated) configuration, $\mathscr{B}^I$, is obtained by filling the canulae with a fluid at pressure p_i, which produces uniform inflation of the gauge section. Here the inner and outer radii become a and b, respectively, in compliance with the customary representation of the deformed configuration variables. The material point X is now at the location $\boldsymbol{x} = r\boldsymbol{e}_r + z\boldsymbol{e}_z$, where $r = r(R)$ and $z = \lambda_z\, Z$ are the deformed coordinates.

An exact expression of the deformed radius can be obtained by virtue of the incompressibility of material, that reads

$$r^2 = a^2 + \lambda_z^{-1}(R^2 - A^2) \tag{4}$$

This can be used as an exact solution of the radial deformation provided

that the deformed inner radius, a is determined from equilibrium equations in section 2.2.

The role of fibers and the anisotropy induced by them in a micro-mechanically based model is expressed elegantly by the formulation in Holzapfel et al. (2000). It is assumed that at least two fiber families exist symmetrically oriented at angles $\pm\phi$ from the circumferential direction, the unit vectors of which are $\boldsymbol{M}$ and $\boldsymbol{M'}$ as shown in Figure 4. The constituent ground and fiber phases are additively decomposed in terms of the corresponding SED expressions

$$\mathscr{W}_m = (1-2\alpha)\mathscr{W}_g + \alpha\mathscr{W}_f + \alpha\mathscr{W}_{f'} \tag{5}$$

where prime indicates the corresponding fiber family. The ground substance was simply modeled as a neo-Hookean material as

$$\mathscr{W}_g = \frac{\mu}{2}(I_1 - 3) \tag{6}$$

where μ represents the shear modulus, while the constitutive model of the fiber phase is defined as

$$\mathscr{W}_f = \frac{k_1}{2k_2}\left\{e^{k_2(I_4-1)^2} - 1\right\} \tag{7}$$

where k_1 has units of force per area and k_2 has no units.

2.2. Parameter estimation procedure based on inverse elasticity

An exact solution of the deformed internal radius, (a in Eq. 4) is required in an inverse elasticity framework set up to determine it's value in the undeformed state, A, and then fit the SED function parameters corresponding to

the simple (Eq.1 for A and k) and the micro-mechanically based (Eq.5 for μ, k_1, and k_2) models, consecutively.

The derivation of the analytical form is only shown for the micro-mechanically based SED function, for which the Cauchy stress components are

$$\begin{aligned}\sigma_{rr} &= (1-2\alpha)(-p+\mu\lambda_r^2)\\ \sigma_{\theta\theta} &= (1-2\alpha)(-p+\mu\lambda_\theta^2)+2\alpha\beta_\theta\lambda_\theta^2\end{aligned} \tag{8}$$

where $\beta_\theta = 2k_1(I_4-1)e^{k_2(I_4-1)^2}\cos^2\phi$. Cauchy's equation of motion in the radial direction reads

$$\frac{\partial\sigma_{rr}}{\partial r}+\frac{1}{r}(\sigma_{rr}-\sigma_{\theta\theta})=0 \tag{9}$$

Applying the chain rule to write the derivative in terms of R and substitution of the stress components σ_{rr} and $\sigma_{\theta\theta}$ from Eq. 8, the above equation reduces to a first order ordinary differential equation of the hydrostatic pressure reading

$$\frac{\mathrm{d}p}{\mathrm{d}R}=\frac{\lambda_r}{r}\left[\mu(\lambda_r^2-\lambda_\theta^2)-\frac{2\alpha\beta_\theta}{1-2\alpha}\lambda_\theta^2\right]+\mu\frac{\mathrm{d}(\lambda_r^2)}{\mathrm{d}R} \tag{10}$$

Upon integrating Eq. 10 from the inner wall $R=A$ to an arbitrary radial location R, we get

$$p(R)=\int_A^R\frac{\lambda_r}{r}\left[\mu(\lambda_r^2-\lambda_\theta^2)-\frac{2\alpha\beta_\theta}{1-2\alpha}\lambda_\theta^2\right]\mathrm{d}R+\mu\left(\lambda_r^2-\lambda_r^2\big|_A\right)+p(A) \tag{11}$$

The integration constant $p(A)$ is evaluated by using the traction boundary

condition at the inner wall $\sigma_{rr}\big|_{R=A} = -p_i$ as

$$p(A) = \mu\lambda_r^2\big|_A + \frac{p_i}{1-2\alpha} \tag{12}$$

Finally, the other traction-free boundary condition at the outer wall $\sigma_{rr}\big|_{R=B} = 0$ results in an integral equation

$$F(\mu, k_1, k_2; a) = \int_A^B \frac{\lambda_r}{r}\left[(1-2\alpha)\mu(\lambda_r^2 - \lambda_\theta^2) - 2\alpha\beta_\theta\,\lambda_\theta^2\right] \mathrm{d}R + \, p_i = 0 \tag{13}$$

which we be solved for a. The parameter estimation procedure outlined in Algorithm 1 uses this equation to solve for the inner radii $\{a_j^n\}$ at the n^{th} iteration corresponding to the internal pressures $p_{i,j}^{\text{Exp}}$ observed in the experiment for N data points.

A nonlinear algebraic solver in Octave Eaton (2022) (`fsolve`) is utilized for this purpose. The search for the best parameters is performed by using the `lsqnonlin` function in Octave. Numerical quadrature was employed in evaluating the functional F.

The parameter estimation procedure shown in Algorithm 1 can be applied to experimental data if the tensile response data is available. If it is missing or incomplete we propose a way to recover the missing part based on the existing data in the next section.

2.3. Inverse deformation based configuration recovery

In vitro pressure-diameter data are seldom provided in the literature. As a consequence, the fitting process may be greatly hindered. We propose to circumvent this difficulty by applying an inverse kinematic "*pull-back*"

Algorithm 1: The parameter estimation procedure.

Data: $\{b_j^{\text{Exp}}, p_{i,j}^{\text{Exp}}\}$ for $j = 1, \ldots, N$
Fixed: $\{\alpha, \phi\}$;
Variables: $\mathbf{x} = \{\mu, k_1, k_2\}$;
Take an initial guess, $\mathbf{x} \leftarrow \mathbf{x}^0$;
while *residual* $>$ *tolerance*:
    Solve Eq.13 for $\{a_j^n \,\forall\, p_{i,j}^{\text{Exp}}\}$;
    Evaluate $\{b_j^n\}$ using Eq.4;
    $residual = \sqrt{\sum_{j=1}^{N}(b_j^n - b_j^{\text{Exp}})^2}$;
    $\mathbf{x} \leftarrow \mathbf{x}^n$;
end

operation to the tethered state, which shall result in the recovery of the excised state.

To this end, Algorithm 1 was modified to include the pull-back of $\mathscr{B}^T$, the tethered state back to $\mathscr{B}$, the excised (undeformed) state (see Algorithm 2). The pull-back operation simply relies on the equality $\mathrm{d}\boldsymbol{X} = \bar{\boldsymbol{F}}^{-1}\mathrm{d}\bar{\boldsymbol{x}}$, and the entire procedure is illustrated in Figure 2.

3. Results

The material parameters were estimated using the `lsqnonlin` function found in the `optim` Till (2022) package in Octave Eaton (2022) so that the load-displacement curves fitted onto the experimental data points with considerably high coefficients of determination ($R^2 > 0.99$) as shown in Table 1 and Figure 3. It can be seen that using Path-1 and thus not accounting for prior tensile stretching (in the tethered state) results in a much higher stiffness coefficient in comparison with Path-2 where pull-back is used to recover the undeformed state.

Algorithm 2: The parameter estimation algorithm including the pull-back operation

Data: $\{b_j^{\text{Exp}}, p_{i,j}^{\text{Exp}}\}$ for $j = 1, \ldots, N$
Fixed: $\{\alpha, \phi\}$;
Variables: $\mathbf{x} = \{\mu, k_1, k_2\}$;
Take an initial guess, $\mathbf{x} \leftarrow \mathbf{x}^0$;
Take an initial guess, $A \leftarrow A^0$;
while *residual* $>$ *tolerance*:
  pull-back to recover A^n, calculate B^n;
  $A \leftarrow A^n$;
  Solve Eq.13 for $\{a_j^n \,\forall\, p_{i,j}^{\text{Exp}}\}$;
  Evaluate $\{b_j^n\}$ using Eq.4;
  $residual = \sqrt{\sum_{j=1}^{N}(b_j^n - b_j^{\text{Exp}})^2}$;
  $\mathbf{x} \leftarrow \mathbf{x}^n$;
end

Table 1: Material parameter estimates from the simulation pair (utilizing the direct and pull-back paths) as well as the reported values in Simon (1972).

Process	$\mathscr{A}$ (kPa)	k	R^2
Simon et al.	9.9	2.1	0.9836
Path-1	12.4	1.78	0.9907
Path-2	4.4	1.71	0.9906

Table 2: Comparison of measured and simulated (Path-2) outer radii. * from the value provided in the Conclusion of Simon et al. (1971). ** Computed.

Configuration	Outer radius (mm)	
	Experimental	Computed
Excised	3.90*	3.91**
Tethered	3.16	3.16
Inflated	5.30	5.32

Table 3: Parameters obtained from data fitting.

ϕ	μ (kPa)	k_1 (kPa)	k_2	R^2
$\pi/6$	14.7	79.2	0.884	0.992
$\pi/4$	31.4	38.6	2.49	0.991
$\pi/3$	34.2	1.68	4.24	0.991

The excised (undeformed) geometry estimate by using the pull-back agreed with the excised state mentioned in Simon et al. (1971), as shown in Table 2.

The response curves obtained from different material parameter sets using the simple material model are presented in Figure 3. Alternatively, parameter fits of the micro mechanically based material model by Holzapfel et al. (2000) are shown in 4. In the latter model, three fiber angle orientations were tried ($\phi = \pi/3$, $\pi/4$, $\pi/6$). The resulting parameter sets are shown in Table 3.

For further examination of the effect of the fiber angle on the constitutive parameters, the Finite Element Analysis Program (FEAP) Taylor and Govindjee (2020) was used to simulate the mechanical behavior of an arterial segment geometry estimated by the pull-back algorithm. Three models corresponding to different fiber orientations ($\pi/3$, $\pi/4$, $\pi/6$) having different

(undeformed) geometries were set up. Loading was incrementally applied in two stages, tethering (extension ratio $\lambda_z = 1.53$) and inflation ($p_i^{max} = 26.6$ kPa) as shown in Figure 5.

The change in wall thickness between loading states, especially the reduction in thickness during the inflation process can be visually recognised from the meshes, as well as seen by looking at the nodal displacement values in Figure 6. A high correlation between the finite element and analytical results was observed.

By virtue of the finite element model, extraction of other variables of interest such as the tethering reaction force and the accumulated strain energy was possible. The reaction force in Figure 7a and the total strain energy in Figure 7b are plotted on the vertical axis, as a function of loading along the horizontal axis.

4. Discussion

The mechanical changes of artery wall is directly related to the cardiovascular diseases which are estimated to end over 17.9 million lives each year and the leading cause of death globally (WHO, https://www.who.int/en/news-room/fact-sheets/detail/cardiovascular-diseases). Constitutive model based interpretation in normal physiology and psychophysiology is an important tool to determine the mechanical characteristics of arteries which cannot be measured in *in vivo*. Constitutive models can generate direct mechanistic and quantitative link between arterial properties which effect clinical stiffness measures. In addition, determination of constitutive model parameters can contribute to the detection of cardiovascular diseases at early stage.

Therefore, the correct estimation and reproduciblity of material parameters based on constitutive models might have critical importance to define clinical reference values for normal and disease state.

In this study, the proposed identification algorithm with pull-back (Alg. 2) is proved to characterise the material properties of an arterial segment with a proper micromechanical model. This algorithm also has the ability to make an accurate guess of the unknown excised radii. We showed that the recovered outer radius of the artery in the excised state agrees very well with the value reported in Simon et al. (1971) (see Table 2). In addition, the material parameters of an arterial segment were extracted with the novel identification algorithm proposed, which used genetic algorithm to produce initial guesses for the nonlinear least squares algorithm. This two step procedure mitigated the overfitting and converged to physiologically sensible parameters with a high coefficient of determination above 0.99. In addition, using Path-1 resulted in a much higher stiffness coefficient in comparison with Path-2 where pull-back was used to recover the undeformed state.

The assumption of three different fiber angle orientations ($\phi = \pi/3$, $\pi/4$, $\pi/6$) demonstrated a proportional relation between the ϕ, and the matrix material stiffness, μ (Table 3). Conversely, the infinitesimal elastic coefficient of the fibers, k_1, changed inversely proportional with ϕ. It could be argued that increasing the stiffness of ground substance tolerates the insufficiency of axially leaned fibers to carry radial pressure loads. It can also be deduced that the exponential stiffening parameter of the fibers, k_2, also increases with ϕ in order to resist shape change at elevated inflation pressures. A decrement in fiber stiffness is expected for the fiber angles that are closer to the axial

direction, to allow for the axial stretching.

Furthermore, the agreement between the computational and analytical solution approved the validity of our identification algorithm with pull-back. The cylinder with a smaller fiber angle appeared to have the smallest undeformed radii among the rest, which meant that it had the smallest radial deformation during the tethering stage. The largest undeformed radii occurred for $\phi = \pi/4$, which deformed more than the others during tethering. The axial force generated during inflation was shown to vary as a function of the fiber orientation, where larger fiber angles resulted in higher tethering reactions, thus pointing to higher axial stiffness. In contrast, fibers which leaned tangentially showed much less resistance to axial stretching. This outcome might be insightful where the axial reaction force of an artery cannot be measured directly.

In fitting the material parameters of an artery from a pressure myogrpahy experiment there are certain difficulties and limitations that need to be addressed. The most important difficulties were found to be the lack of experimental data such as the tethering force, lack of measurement of the undeformed geometry, high variability (standard deviation) among independent experimental measurements, the geometric non-uniformity of the vessels in contrast with the analytical models. As a result, a high potential of overfitting naturally arises in the material parameter fitting procedure. Thus, our procedure might serve to predict consistent material parameters that can be reproduced from various pressure myography experiments.

5. Acknowledgement

This work was funded by Scientific and Technological Research Council of Türkiye (TUBITAK) grant number 221S551.

6. Declaration of Competing Interest

The authors declare that they have no known competing financial interests or personal relationships that could have appeared to influence the work reported in this paper.

7. Credit authorship contribution statement

OFB: Optimization method search, literature survey, investigation, writing of the original draft version, **CVK:** Optimization method search, methodology, software, verification of numerical results, **BGT:** Investigation of physiological behavior, methodology, review and editing of the manuscript, **AFO:** Conceptualization, methodology, investigation, writing, reviewing and editing of the manuscript.

References

Avril, S., Badel, P., Duprey, A., 2010. Anisotropic and hyperelastic identification of in vitro human arteries from full-field optical measurements. Journal of Biomechanics 43, 2978–2985. URL: http://www.sciencedirect.com/science/article/pii/S0021929010003738 www.elsevier.com/locate/jbiomech, doi:10.1016/j.jbiomech.2010.07.004.

Cheung, J.B., Hsiao, C.C., 1972. Nonlinear anisotropic viscoelastic stresses in blood vessels. Journal of Biomechanics 5, 607–619. doi:10.1016/0021-9290(72)90033-4.

Chuong, C.J., Fung, Y.C., 1983. Three-dimensional stress distribution in arteries. journal of biomechanical engineering 105, 268–274. URL: http://biomechanical.asmedigitalcollection.asme.org/.

Chuong, C.J., Fung, Y.C., 1986. On residual stresses in arteries. Journal of Biomechanical Engineering 108, 189–192. URL: http://asmedigitalcollection.asme.org/biomechanical/article-pdf/108/2/189/566580 doi:10.1115/1.3138600.

Demiray, H., 1972. A note on the elasticity of soft biological tissues. Journal of Biomechanics 5, 309–311. doi:10.1016/0021-9290(72)90047-4.

Dobrin, P.B., 1984. Mechanical behavior of vascular smooth muscle in cylindrical segments of arteries in vitro. Annals of Biomedical Engineering 12, 497–510. doi:10.1007/BF02363919.

Eaton, J.W., 2022. Gnu octave 7.2.0 user manual. Accessed on July 23,2022.

Einstein, D.R., Freed, A.D., Stander, N., Fata, B., Vesely, I., 2005. Inverse parameter fitting of biological tissues: A response surface approach. Annals of Biomedical Engineering 33, 1819–1830. doi:10.1007/s10439-005-8338-3.

Fung, Y.C., Fronek, K., Patitucci, P., 1979. Pseudoelasticity of arteries and the choice of its mathematical expression. American Journal of Physiology - Heart and Circulatory Physiology 6. doi:10.1152/ajpheart.1979.237.5.H620.

Garcia-Gonzalez, D., Jérusalem, A., Garzon-Hernandez, S., Zaera, R., Arias, A., 2018. A continuum mechanics constitutive framework for transverse isotropic soft tissues. Journal of the Mechanics and Physics of Solids 112, 209–224. URL: https://doi.org/10.1016/j.jmps.2017.12.001, doi:10.1016/j.jmps.2017.12.001.

Genovese, K., 2007. Radial metrology application to whole-body measurement on hyperelastic tubular samples. Optics and Lasers in Engineering 45, 1059–1066. doi:10.1016/j.optlaseng.2007.05.003.

Genovese, K., 2009. A video-optical system for time-resolved whole-body measurement on vascular segments. Optics and Lasers in Engineering 47, 995–1008. URL: http://www.sciencedirect.com/science/article/pii/S0143816609001006, doi:10.1016/j.optlaseng.2009.04.017.

Hayashi, K., 1993. Experimental approaches on measuring the mechanical properties and constitutive laws of arterial walls. Journal of Biomechanical Engineering 115, 481–488. doi:10.1115/1.2895528.

Hayashi, K., Sato, M., Handa, H., Moritake, K., 1974. Biomechanical study of the constitutive laws of vascular walls. Experimental mechanics 14, 440–444.

Heagerty, A.M., Aalkjær, C., Bund, S.J., Korsgaard, N., Mulvany, M.J., 1993. Small artery structure in hypertension: Dual processes of remodeling and growth. Hypertension 21, 391–397. doi:10.1161/01.HYP.21.4.391.

Holzapfel, G., 2000. Nonlinear solid mechanics: a continuum approach for engineering. Wiley and Sons.

Holzapfel, G.A., Gasser, T.C., Ogden, R.W., 2000. A new constitutive framework for arterial wall mechanics and a comparative study of material models. Journal of elasticity and the physical science of solids 61, 1–48.

Holzapfel, G.A., Gasser, T.C., Ogden, R.W., 2004. Comparison of a multilayer structural model for arterial walls with a fung-type model, and issues of material stability. Journal of biomechanical engineering 126, 264–275. doi:10.1115/1.1695572.

Huh, U., Lee, C.W., You, J.H., Song, C.H., Lee, C.S., Ryu, D.M., 2019. Determination of the material parameters in the holzapfel-gasser-ogden constitutive model for simulation of age-dependent material nonlinear behavior for aortic wall tissue under uniaxial tension. Applied Sciences (Switzerland) 9. doi:10.3390/app9142851.

Irgens, F., 2008. Continuum mechanics. Springer Science & Business Media.

Kang, T., 2008. Mechanical behavior of arteries under inflation and extension. Journal of Mechanical Science and Technology 22, 621. URL: https://doi.org/10.1007/s12206-008-0213-3, doi:10.1007/s12206-008-0213-3.

Kas'yanov, V.A., 1974. Anisotropic nonlinear-elastic model of the large human blood vessels. polymer mechanics 10, 756–764.

Lakatta, E.G., Wang, M., Najjar, S.S., 2009. Arterial aging and subclinical arterial disease are fundamentally intertwined at macroscopic

and molecular levels. Medical Clinics of North America 93, 583–604. doi:10.1016/j.mcna.2009.02.008.

Leblanc, C., Strong, H.R., Tabrizchi, R., 2018. Evaluation of different metrics as an index for the assessment of arterial stiffness. Clinical and Experimental Hypertension 40, 390–397. doi:10.1080/10641963.2017.1384484.

Lee, H.Y., Oh, B.H., 2010. Aging and arterial stiffness. Circulation Journal 74, 2257–2262. doi:10.1253/circj.CJ-10-0910.

Mackerle, J., 2005. Finite element modelling and simulations in cardiovascular mechanics and cardiology: A bibliography 1993–2004. Computer Methods in Biomechanics and Biomedical Engineering 8, 59–81. doi:10.1080/10255840500141486.

Mazier, A., Bilger, A., Forte, A.E., Peterlik, I., Hale, J.S., Bordas, S.P., 2022. Inverse deformation analysis: an experimental and numerical assessment using the fenics project. Engineering with Computers doi:10.1007/s00366-021-01597-z.

Mirsky, I., 1973. Ventricular and arterial wall stresses based on large deformation analyses. Biophysical Journal 13, 1141–1159. doi:10.1016/S0006-3495(73)86051-5.

Mitchell, G.F., Guo, C.Y., Benjamin, E.J., Larson, M.G., Keyes, M.J., Vita, J.A., Vasan, R.S., Levy, D., 2007. Cross-sectional correlates of increased aortic stiffness in the community: The framingham heart study. Circulation 115, 2628–2636. doi:10.1161/CIRCULATIONAHA.106.667733.

Morin, C., Avril, S., 2015. Inverse problems in the mechanical characterization of elastic arteries. MRS Bulletin 40, 317–323. doi:10.1557/mrs.2015.63.

Myneni, M., Rajagopal, K.R., 2022. Constitutive modeling of the mechanical response of arterial tissues. Applications in Engineering Science 11. doi:10.1016/j.apples.2022.100111.

Nair, S., 2009. Introduction to Continuum Mechanics. Cambridge University Press. doi:10.1017/CBO9780511841576.

Ogden, R.W., Saccomandi, G., Sgura, I., 2004. Fitting hyperelastic models to experimental data. Computational Mechanics 34, 484–502. URL: https://doi.org/10.1007/s00466-004-0593-y, doi:10.1007/s00466-004-0593-y.

Ramachandra, A., Humphrey, J.D., 2019. Biomechanical characterization of murine pulmonary arteries. Journal of Biomechanics 84, 18–26. doi:10.1016/j.jbiomech.2018.12.012.

s. Roy, C., 1881. The elastic properties of the arterial wall. Journal of physiology .

Sell, D.R., Monnier, V.M., 2012. Molecular basis of arterial stiffening: Role of glycation-a mini-review. Gerontology 58, 227–237. doi:10.1159/000334668.

Simon, B.R., Kobayashi, A.S., Strandness, D.E., Wiederhielm, C.A., 1971. Large deformation analysis of the arterial cross section. Journal of Fluids Engineering, Transactions of the ASME 93, 138–145. doi:10.1115/1.3425199.

Simon, B.R., Kobayashi, A.S., Strandness, D.E., Wiederhielm, C.A., 1972. Reevaluation of arterial constitutive relations. a finite-deformation approach. Circulation research 30, 491–500. doi:10.1161/01.RES.30.4.491.

Sleboda, D.A., Roberts, T.J., 2017. Incompressible fluid plays a mechanical role in the development of passive muscle tension. Biology Letters 13, 20160630. doi:10.1098/rsbl.2016.0630.

Taira, S., Hayashi, K., Sato, M., 1974. Biomechanical study of vascular walls (stress analysis of vascular walls by finite element method). Journal of the Society of Materials Science, Japan 23, 437–443.

Taylor, R.L., Govindjee, S., 2020. Feap -finite element analysis program, v8.6 user manual. Accessed on Aug,1,2017.

Till, O., 2022. Gnu octave – non-linear optimization package v1.6.2 user manual. Accessed on Aug. 1,2022.

Ungvari, Z., Tarantini, S., Donato, A.J., Galvan, V., Csiszar, A., 2018. Mechanisms of vascular aging. Circulation Research 123, 849–867. URL: https://doi.org/10.1161/CIRCRESAHA.118.311378, doi:10.1161/CIRCRESAHA.118.311378.

Vaishnav, R.N., Young, J.T., Patel, D.J., 1973. Distribution of stresses and of strain energy density through the wall thickness in a canine aortic segment. Circulation Research 32, 577–583. doi:10.1161/01.RES.32.5.577.

Vito, R.P., Hickey, J., 1980. The mechanical properties of soft tissues-ii : The elastic response of arterial segments*. journal of biomechanics 13, 951–957.

Wex, C., Arndt, S., Stoll, A., Bruns, C., Kupriyanova, Y., 2015. Isotropic incompressible hyperelastic models for modelling the mechanical behaviour of biological tissues: A review. Biomedizinische Technik 60, 577–592. URL: https://www.degruyter.com/view/journals/bmte/60/6/article-p577.xml, doi:10.1515/bmt-2014-0146.

Wicker, B.K., Hutchens, H.P., Wu, Q., Yeh, A.T., Humphrey, J.D., 2008. Normal basilar artery structure and biaxial mechanical behaviour. Computer Methods in Biomechanics and Biomedical Engineering 11, 539–551. doi:10.1080/10255840801949793.

Wu, S.G., Lee, G.C., Tseng, N.T., 1984. Nonlinear elastic analysis of blood vessels. Journal of Biomechanical Engineering 106, 376–383. doi:10.1115/1.3138509.

Young, J.T., Vaishnav, R.N., Patel, D.J., 1977. Nonlinear anisotropic viscoelastic properties of canine arterial segments. Journal of Biomechanics 10, 549–559. doi:10.1016/0021-9290(77)90035-5.

Zulliger, M.A., Rachev, A., Stergiopulos, N., 2004. A constitutive formulation of arterial mechanics including vascular smooth muscle tone. American Journal of Physiology - Heart and Circulatory Physiology 287, 1335–1343. URL: http://www.ajpheart.org, doi:10.1152/ajpheart.00094.2004.

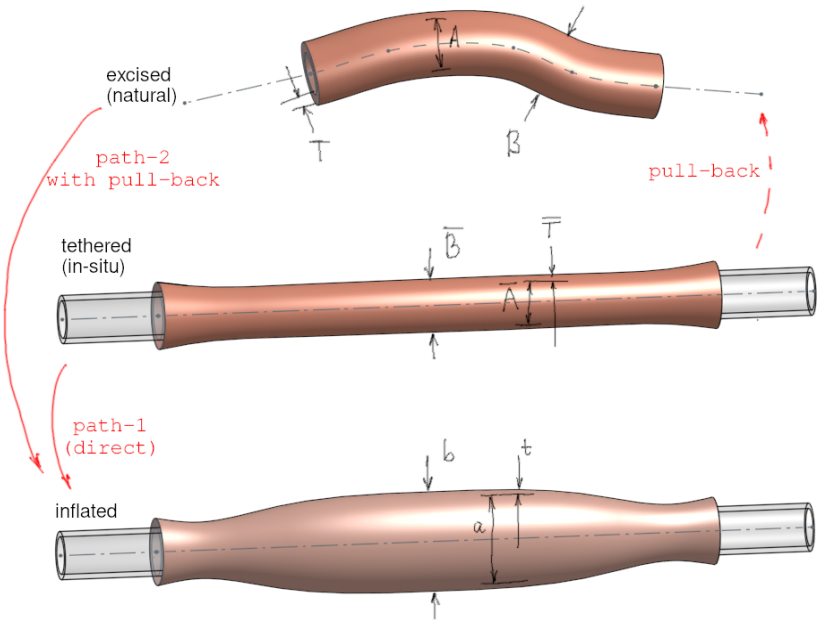

Figure 1: The three standard specimen configurations in a pressure-myography experiment. From left to right, excised (E), tethered between canulae (T), and inflated (I)

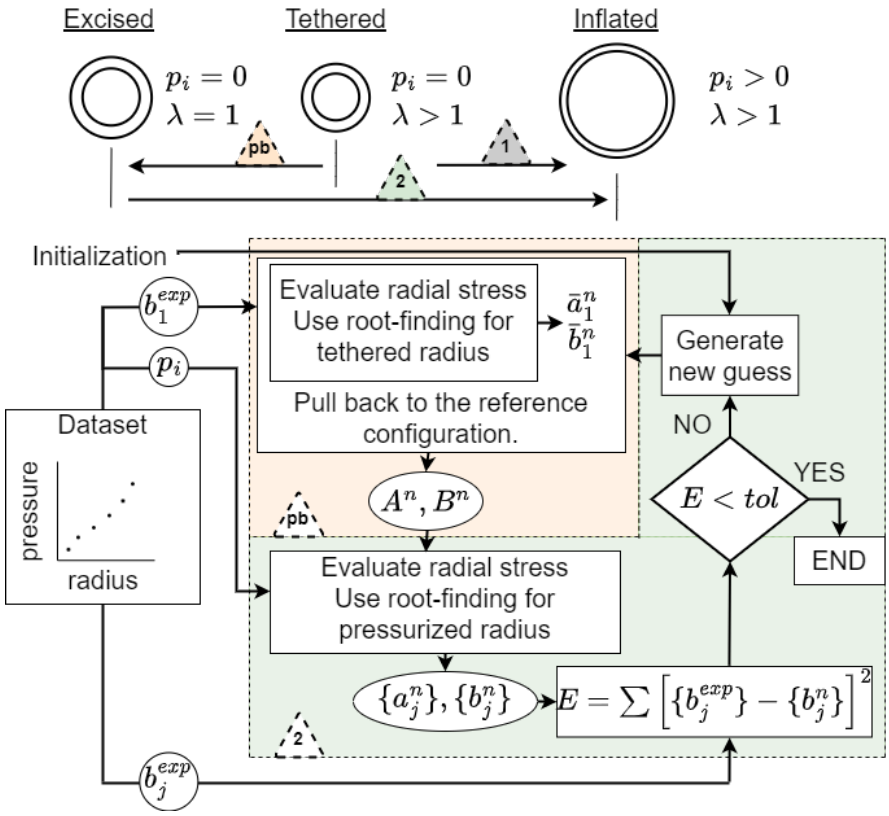

Figure 2: The parameter estimation procedure to obtain the least-square fit parameter values, including the pull-back operation

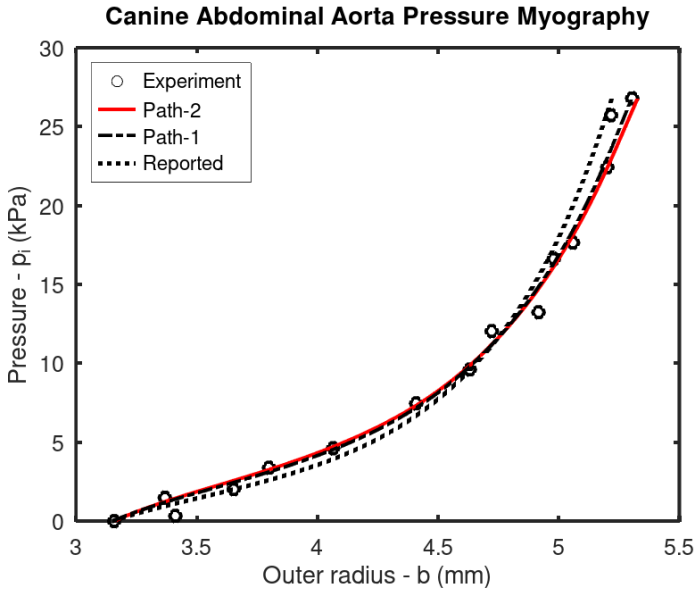

Figure 3: Mechanical response curves obtained using different procedures

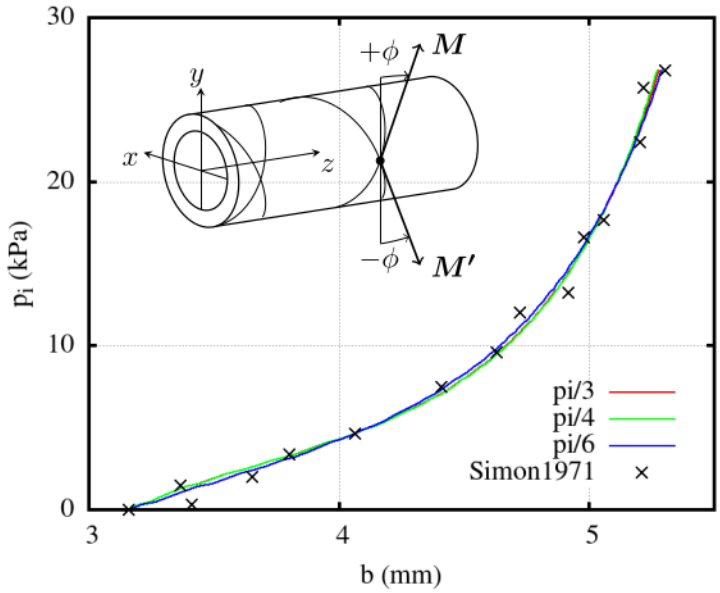

Figure 4: Material parameter fits for $\phi = \{\pi/6, \pi/4, \pi/3\}$

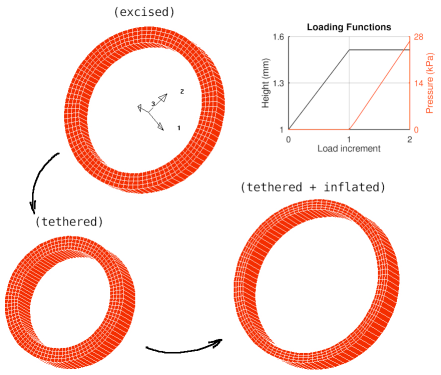

Figure 5: Depiction of the finite element artery slice model and its deformed states resulting from the applied loading (top left)

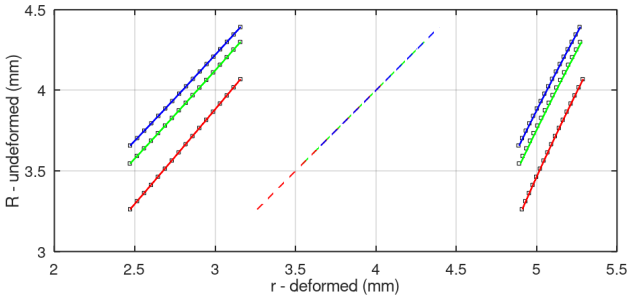

Figure 6: Deformation mapping from reference configuration to the deformed.
The mapping is shown at three states (loadsteps): excised (loadstep zero) in middle, tethered (loadstep one) on left, inflated (loadstep two) on right. Red, blue and green lines represent the models with $\phi = \pi/6$, $\phi = \pi/4$ and $\phi = \pi/3$, respectively. Lines are from the analytical model whereas points are from the finite element analysis

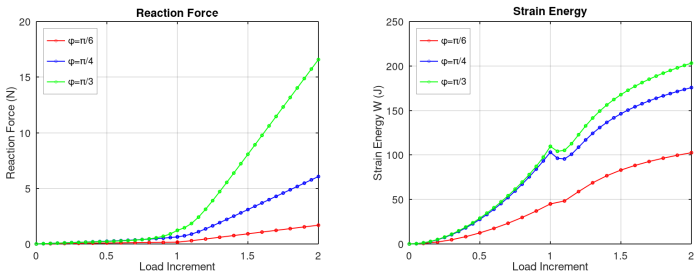

(a) (b)

Figure 7: The changes in the tethering reaction force (a) and total strain energy (b) in the model as a function of load increments.

Figure Captions

1. The three standard specimen configurations in a pressure-myography experiment. From left to right, excised (E), tethered between canulae (T), and inflated (I)
2. The parameter estimation procedure to obtain the least-square fit parameter values, including the pull-back operation
3. Mechanical response curves obtained using different procedures.
4. Material parameter fits for $\phi = \{\pi/6, \pi/4, \pi/3\}$
5. Depiction of the finite element artery slice model and its deformed states resulting from the applied loading (top left)
6. The mapping is shown at three states (loadsteps): excised (loadstep zero) in middle,

   tethered (loadstep one) on left, inflated (loadstep two) on right. Red, blue and green lines represent the models with $\phi = \pi/6$, $\phi = \pi/4$ and $\phi = \pi/3$, respectively. Lines are from the analytical model whereas points are from the finite element analysis
7. The changes in the tethering reaction force (a) and total strain energy in the model as a function of load increments.